

Spectroscopic Confirmation of an Ultra-Faint Galaxy at the Epoch of Reionization

Austin Hoag^{1*}, Maruša Bradač¹, Michele Trenti²,
Tommaso Treu³, Kasper B. Schmidt⁴, Kuang-Han Huang¹, Brian C. Lemaux¹,
Julie He¹, Stephanie R. Bernard², Louis E. Abramson³, Charlotte A. Mason^{3,5},
Takahiro Morishita^{3,6,7}, Laura Pentericci⁸, and Tim Schrabback⁹

¹Department of Physics, University of California, Davis, CA 95616

²School of Physics, University of Melbourne, VIC 3010, Australia

³Department of Physics and Astronomy, University of California, Los Angeles, CA 90095

⁴Leibniz-Institut für Astrophysik Potsdam (AIP), An der Sternwarte 16, 14482 Potsdam, Germany

⁵Department of Physics, University of California, Santa Barbara, CA 93106-9530, USA

⁶Astronomical Institute, Tohoku University, Aramaki, Aoba, Sendai 980-8578, Japan

⁷Institute for International Advanced Research and Education,
Tohoku University, Aramaki, Aoba, Sendai 980-8578, Japan

⁸INAF Osservatorio Astronomico di Roma, Via Frascati 33,
I-00040 Monteporzio (RM), Italy

⁹ Argelander-Institut für Astronomie, Auf dem Hügel 71, D-53121 Bonn, Germany

*To whom correspondence should be addressed; E-mail: athoag@ucdavis.edu.

Within one billion years of the Big Bang, intergalactic hydrogen was ionized by sources emitting ultraviolet and higher energy photons. This was the final phenomenon to globally affect all the baryons (visible matter) in the Universe. It is referred to as cosmic reionization and is an integral component of cosmology. It is broadly expected that intrinsically faint galaxies were the primary ionizing sources due to their abundance in this epoch. However, at the highest redshifts ($z > 7.5$; lookback time 13.1 Gyr), all galaxies with spectroscopic confirmations to date are intrinsically bright and therefore not necessarily representative of the general population. Here we report the unequivocal spectroscopic detection of a low luminosity galaxy at $z > 7.5$. We detected the Lyman-alpha ($\text{Ly}\alpha$) emission line at $\sim 10504\text{\AA}$ in two separate observations

with MOSFIRE on the Keck I Telescope and independently with the *Hubble* Space Telescope slit-less grism spectrograph, implying a source redshift of $z = 7.640 \pm 0.001$. The galaxy is gravitationally magnified by the massive galaxy cluster MACS J1423.8+2404 ($z = 0.545$), with an estimated intrinsic luminosity of $M_{\text{AB}} = -19.6 \pm 0.2$ mag and a stellar mass of $M^* = 3.0_{-0.8}^{+1.5} \times 10^8$ solar masses. Both are an order of magnitude lower than the four other Ly α emitters currently known at $z > 7.5$, making it probably the most distant representative source of reionization found to date.

We originally identified the galaxy (MACS1423-z7p64, hereafter), as a $z > 7$ candidate in [1] using imaging from the Cluster Lensing And Supernova survey with *Hubble* [2] (CLASH). In [1], we also reported a tentative $\sim 2\sigma$ detection of the hydrogen Lyman-alpha (Ly α) emission line at $10500 \pm 50\text{\AA}$ using slit-less spectroscopy from the Grism Lens-Amplified Survey from Space [3, 4] (GLASS; GO-13459, Principal Investigator PI T. Treu). In this work, we present ground-based spectroscopic follow-up of MACS1423-z7p64 obtained with the Multi-Object Spectrometer for Infra-Red Exploration [5] (MOSFIRE) on the Keck I Telescope on Mauna Kea, HI, on 27 May 2015 (PI M. Bradač; 2.3 hrs) and 19 March 2016 (PI M. Trenti; 1.85 hrs).

Figure 1 shows the one- and two-dimensional co-added Keck/MOSFIRE spectrum. An emission line is detected at 10504\AA with a signal-to-noise ratio (S/N) of 6.7. The implied redshift of the galaxy from the MOSFIRE spectrum is $z = 7.640 \pm 0.001$, placing it in the top five most distant Ly α emitters. The wavelength of the line in the MOSFIRE spectrum is consistent with the wavelength of the emission line in the lower resolution *Hubble* Space Telescope (*HST*) G102 grism spectrum from GLASS (Figure 2). The Ly α line flux from MOSFIRE is $0.41 \pm 0.06 \times 10^{-17}$ erg/s/cm². Using the *HST* F125W broadband magnitude ($m_{\text{AB}} = 25.32 \pm 0.11$) to estimate the rest-frame ultraviolet (UV) continuum, we measure a rest-frame equivalent width of $W_{\text{Ly}\alpha} = 9 \pm 2$ Å from the MOSFIRE spectrum.

We show cutouts of MACS1423-z7p64 in seven *HST* filters and the *Spitzer*/IRAC [3.6] μm and [4.5] μm bands in Figure 3a. The source is detected in F125W, F140W and F160W and exhibits a sharp drop in flux in F105W, consistent with a galaxy spectrum at $z = 7.640$ (Figure 3d). We also show a near-infrared false-color *HST* image of MACS1423-z7p64 and the foreground galaxy cluster lens at $z = 0.545$ in Figure 3b. The white line, called the critical line, indicates an infinitesimal band of maximum magnification for sources at $z = 7.640$, the redshift of MACS1423-z7p64. The critical line is very elliptical, a characteristic shared with many other excellent cosmic lenses, and extends to within a few arc seconds of MACS1423-z7p64. Using the lens modeling software SWUnited [6], we determined that the cluster magnifies MACS1423-z7p64 by a factor of $9.6_{-1.6}^{+1.8}$ (68% confidence), equivalent to ~ 2.5 magnitudes. As a result, the intrinsic luminosity of the galaxy at a rest-frame of 1600\AA is $L_{\text{UV}} = 0.4_{-0.1}^{+0.2} L_{\text{UV}}^*$, i.e. 40% of the characteristic luminosity at $z \sim 8$, where we adopted $M_{\text{UV}}^* = -20.63 \pm 0.36$ from [7] to determine L_{UV}^* . We list all photometric and spectroscopic properties of MACS1423-z7p64 in Table 1.

Using the longer wavelength G141 GLASS spectra, we can rule out the [O II] interpreta-

tion of the emission line at $z = 1.818$; if the emission line at 10504\AA was part of the [O II] doublet, then the [O III] pair would have very likely been detected in the G141 spectra (Figure 2; see also Supplementary Information). The [O III] pair is not detected in either P.A., however. Though a sky line in the MOSFIRE spectrum prevents us from reliably measuring the asymmetry often associated with Ly α emission or definitely ruling out the presence of a doublet, photometric constraints also strongly favor the Ly α interpretation at $z = 7.640 \pm 0.001$.

Numerous searches for Ly α at $z > 7$ have been carried out, revealing an extremely low Ly α emitting fraction [8, 9, 10, 1]. We targeted MACS1423-z7p64 along with 9 other $z \gtrsim 7$ candidates in MACS J1423.8+2404 using the selection technique discussed by [1] and as part of a larger ongoing campaign to follow up Ly α emitter candidates from the GLASS program. Of the 9 candidates targeted in MACS J1423.8+2404, only 1 other target with a marginal Ly α detection in the GLASS spectra was observed to the same depth as MACS1423-z7p64, with no evidence of a detection. Therefore, that candidate is likely not a real Ly α emitter, highlighting the importance of follow-up. A full discussion of the ground-based follow up of the GLASS Ly α candidates will be presented by Hoag et al. (in preparation).

Ly α emission has been detected with $S/N > 5$ at $z > 7.5$ in only four other sources, all of which are $L_{UV} > L_{UV}^*$ sources [11, 12, 13, 14], naturally suggesting a relationship between rest-frame UV luminosity and Ly α visibility. It has been proposed by [13, 15] that the preferential success for bright sources could be due to brighter, more massive galaxies tracing the centers of the largest ionized regions, allowing Ly α to redshift out of resonance before encountering intergalactic hydrogen. This model is often referred to as “inside-out” reionization, and is favored by most recent simulations [16, 17]. The detection of Ly α from a single faint galaxy at $z > 7.5$ is not necessarily at odds with this scenario. The size of ionized regions at $z \sim 8$ is typically much larger than the *HST* WFC3/IR field of view (FOV) [18] such that more massive galaxies part of the same ionized region could have escaped our detection. Within the GLASS FOV, several other Ly α candidates also exist, though without full depth follow-up [1].

Another mechanism may be contributing to the visibility of Ly α from MACS1423-z7p64. At least 3 out of the 4 other Ly α emitters at $z > 7.5$ exhibit extremely red rest-frame optical (observed mid-infrared) color, i.e. $([3.6] \mu m - [4.5] \mu m) > 0.5$. For the 4th Ly α emitter presented by [14], the mid-infrared color was not measured due to contamination. Bright [O III] $\lambda\lambda 4959, 5007$ and H β emission lines—which fall in the *Spitzer*/IRAC $[4.5] \mu m$ band at $z \gtrsim 7.1$ and are associated with vigorous star formation—may be responsible for such red colors [19, 20]. The strength of [O III] emission has been linked to hard ionization fields in $z = 3-4$ galaxies by [21] and tentatively at higher redshift by [22], which could also increase the Ly α visibility by clearing away the neutral hydrogen in the local environment. MACS1423-z7p64 is only detected with confidence in the $[4.5] \mu m$ band, such that we measure the mid-infrared color as a 3σ lower limit: $([3.6] - [4.5]) > 0.19$. Therefore, it is possible that the galaxy may exhibit a similarly red color to the other systems mentioned

above. If this were the case, it could indicate a hard ionizing spectrum, explaining why we are able to detect Ly α from this source despite its intrinsically low luminosity, $L_{UV} = 0.4_{-0.1}^{+0.2} L_{UV}^*$, and stellar mass, $3.0_{-0.8}^{+1.5} \times 10^8$ solar masses (M_{\odot}). MACS1423-z7p64 also harbors a very young stellar population (24_{-7}^{+16} Myr), a property it shares with the red mid-infrared galaxies at $z > 7.5$.

An indication that MACS1423-z7p64 may be vigorously forming stars is its large specific star-formation rate (sSFR) implied from spectral energy distribution (SED) fitting: $46.7_{-17.4}^{+19.0} \text{Gyr}^{-1}$. This is comparable to the sSFRs of the 3 Ly α emitters at $z > 7.5$ with measured strong rest-frame optical colors. [22] noted that the red [3.6] – [4.5] μm color at $z > 7.1$ may be due in part to high sSFR. Therefore, the large sSFR implied from SED fitting could imply a harder ionizing spectrum, allowing Ly α to escape.

The *James Webb Space Telescope* (JWST) will be sensitive to the rest-frame UV and optical spectrum of MACS1423-z7p64, making this galaxy an excellent candidate for future follow-up. With modest exposure times, JWST spectroscopic observations could constrain the hardness of the spectrum through rest-frame UV line strengths and measure the [O III]/H β strengths to determine the nature of the flux excess in the *Spitzer*/IRAC [4.5] μm band.

| Photometry | | |
|----------------------------------------------------|---------------------------------------------------|----------------------|
| α_{J2000} | ($^{\circ}$) | 215.942406 |
| δ_{J2000} | ($^{\circ}$) | 24.069655 |
| μ_{best} | | $9.6^{+1.8}_{-1.6}$ |
| $M_{1600} - 2.5\log_{10}(\mu/\mu_{\text{best}})^a$ | (mag) | -19.6 ± 0.2 |
| $M_{\star} \times \mu/\mu_{\text{best}}$ | ($10^8 M_{\odot}$) | $3.0^{+1.5}_{-0.8}$ |
| $\text{SFR} \times \mu/\mu_{\text{best}}$ | $M_{\odot} \text{ yr}^{-1}$ | $13.9^{+4.2}_{-3.8}$ |
| Age | (Myr) | 24^{+16}_{-7} |
| F435W | (mag) | > 26.70 |
| F475W | (mag) | > 26.77 |
| F555W | (mag) | > 27.19 |
| F606W | (mag) | > 27.16 |
| F775W | (mag) | > 26.48 |
| F814W | (mag) | > 27.50 |
| F850LP | (mag) | > 26.24 |
| F105W | (mag) | 26.46 ± 0.24 |
| F110W | (mag) | 25.79 ± 0.11 |
| F125W | (mag) | 25.32 ± 0.11 |
| F140W | (mag) | 24.99 ± 0.06 |
| F160W | (mag) | 25.03 ± 0.10 |
| [3.6] μm | (mag) | > 24.69 |
| [4.5] μm | (mag) | 24.50 ± 0.27 |
| Keck/MOSFIRE Spectroscopy | | |
| $z_{\text{Ly}\alpha}$ | | 7.640 ± 0.001 |
| t_{exp} | (hr) | 4.15 |
| $f_{\text{Ly}\alpha}^{\text{MOSFIRE}}$ | ($10^{-17} \text{ erg s}^{-1} \text{ cm}^{-2}$) | 0.41 ± 0.06 |
| $W_{\text{Ly}\alpha}^{\text{MOSFIRE}}$ | (\AA) | 9 ± 2 |
| Grism Spectroscopy | | |
| $f_{\text{Ly}\alpha}^{\text{PA8}}$ | ($10^{-17} \text{ erg s}^{-1} \text{ cm}^{-2}$) | < 1.35 |
| $f_{\text{Ly}\alpha}^{\text{PA88}}$ | ($10^{-17} \text{ erg s}^{-1} \text{ cm}^{-2}$) | 1.20 ± 0.50 |
| $f_{\text{CIV}}^{\text{PA8}}$ | ($10^{-17} \text{ erg s}^{-1} \text{ cm}^{-2}$) | < 1.17 |
| $f_{\text{CIV}}^{\text{PA88}}$ | ($10^{-17} \text{ erg s}^{-1} \text{ cm}^{-2}$) | < 1.23 |
| $f_{\text{CIII}}^{\text{PA8}}$ | ($10^{-17} \text{ erg s}^{-1} \text{ cm}^{-2}$) | < 1.08 |
| $f_{\text{CIII}}^{\text{PA88}}$ | ($10^{-17} \text{ erg s}^{-1} \text{ cm}^{-2}$) | < 1.23 |
| $W_{\text{Ly}\alpha}^{\text{PA8}}$ | (\AA) | < 30 |
| $W_{\text{Ly}\alpha}^{\text{PA88}}$ | (\AA) | 27 ± 11 |
| $W_{\text{CIV}}^{\text{PA8}}$ | (\AA) | < 30 |
| $W_{\text{CIV}}^{\text{PA88}}$ | (\AA) | < 33 |
| $W_{\text{CIII}}^{\text{PA8}}$ | (\AA) | < 21 |
| $W_{\text{CIII}}^{\text{PA88}}$ | (\AA) | < 24 |

Table 1: Photometric and spectroscopic properties of MACS1423-z7p64. *HST* magnitudes are normalized by the SExtractor MAG AUTO value in F160W, but colors are measured with MAG ISO. All uncertainties are 1σ , whereas upper limits are 3σ . Equivalent widths are calculated using the measured *HST* magnitudes to estimate the continuum flux density. F125W, F160W and F140W are used in the EW calculations for Ly α , C IV and C III], respectively.^a M_{1600} is the rest-frame absolute UV magnitude at 1600 \AA , calculated from the F140W magnitude.

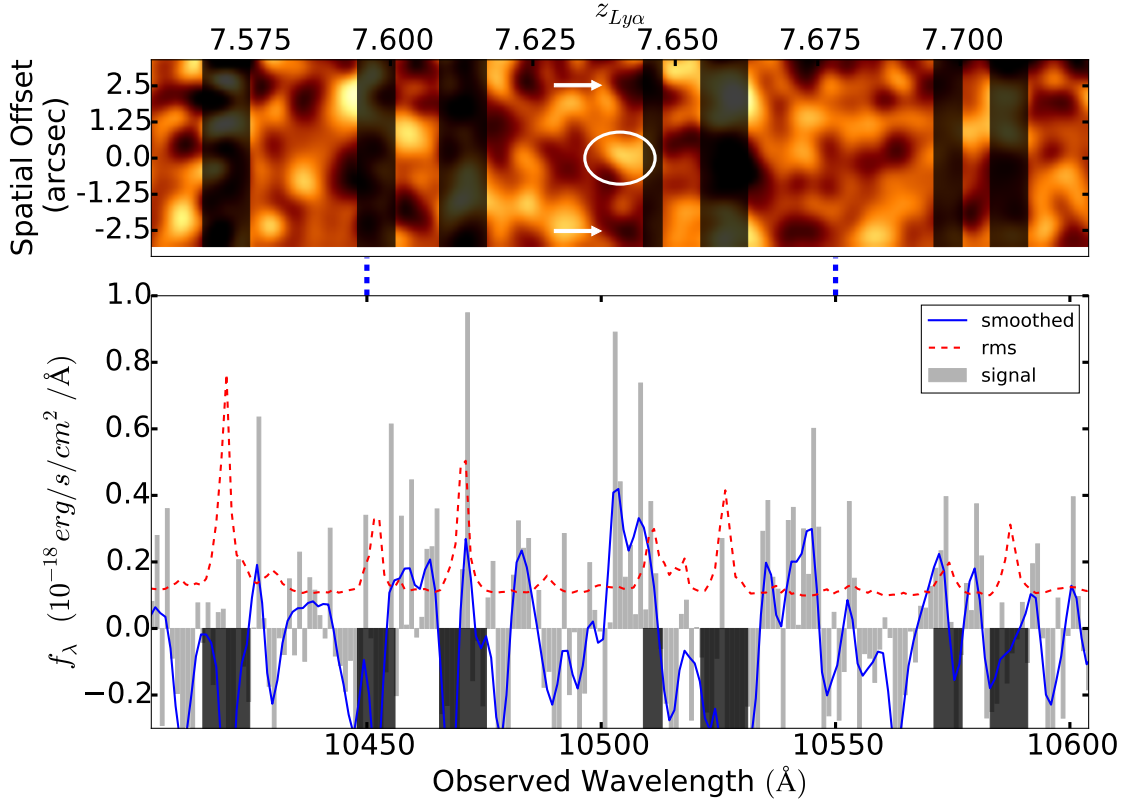


Fig. 1: Integrated $S/N = 6.7$ detection of the $\text{Ly}\alpha$ emission line at $z = 7.640$ with Keck/MOSFIRE. **Top:** Two-dimensional full-depth (4.15 hr) co-added spectrum. The spectrum has been smoothed to the atmospheric seeing of the observations. The emission line is shown inside the white circle for reference, and the white arrows mark the locations of both negative residuals, which appear at the expected locations and with the expected intensities from the dither pattern. **Bottom:** The one-dimensional spectrum extracted from the above two-dimensional spectrum. The signal and rms noise are shown with shaded grey and dotted red lines, respectively. Both are unsmoothed and extracted using the same seeing-matched aperture. The rms noise was obtained from the stacked two-dimensional rms spectrum of the two independent MOSFIRE data sets. The blue line is the signal once smoothed to the MOSFIRE spectral resolution. Atmospheric emission lines are masked out in both panels with dark gray vertical bands. The two dashed vertical blue lines between the top and bottom panels represent the 68% confidence interval for the $\text{Ly}\alpha$ wavelength from the GLASS spectra.

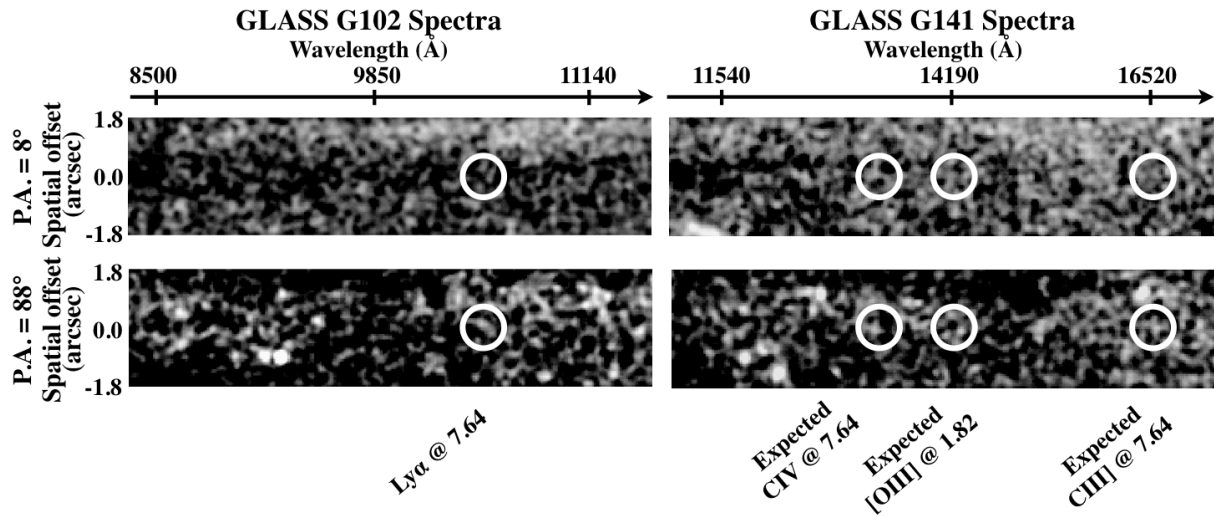


Fig. 2: *HST* G102 (left) and G141 (right) two-dimensional contamination-subtracted spectra from the GLASS program [3, 4]. The two different P.A.s (8° and 88°) are shown in the top and bottom panels, respectively. $\text{Ly}\alpha$ emission is detected with $S/N = 2.4$ at $10500 \pm 50 \text{ \AA}$ in the P.A.= 88° G102 spectrum, and an upper limit is obtained in the P.A.= 8° spectrum, likely due to contamination. The white circles denote the observed $\text{Ly}\alpha$ and the predicted C IV $\lambda\lambda 1548, 1551$ and C III] $\lambda\lambda 1907, 1909$ emission lines at $z = 7.640$. Marginal flux excesses ($< 3\sigma$) are observed for C IV and C III] in the P.A.= 88° G141 spectrum, but follow-up spectroscopy is needed to confirm or deny these features. Also shown is the expected location of the [O III] pair at $z = 1.818$, the redshift if the $\text{Ly}\alpha$ line was instead [O II]. [O III] is not detected assuming $z = 1.818$, which provides strong evidence against the [O II] interpretation of the line because typically $f_{[\text{O III}]} / f_{[\text{O II}]} \geq 1.5$ for low-mass galaxies at this redshift [23].

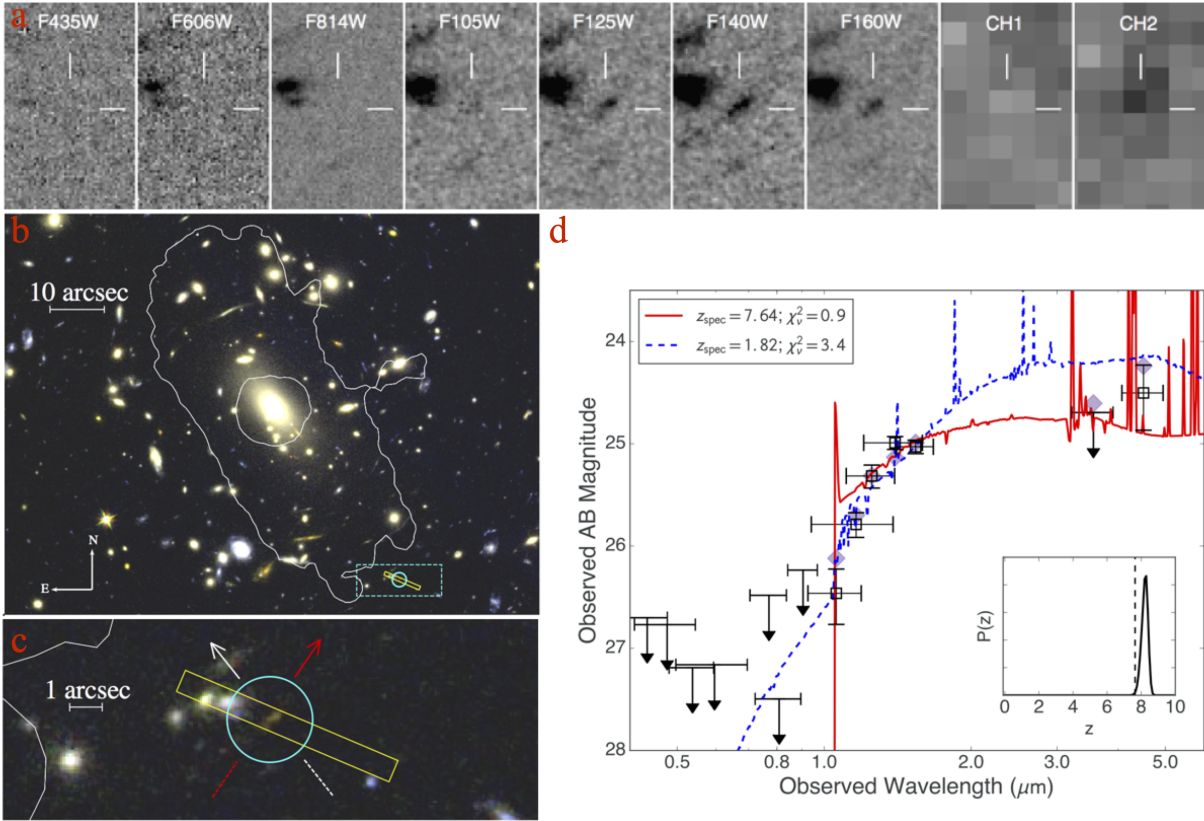


Fig. 3: (a) $3'' \times 5''$ *HST* and background-subtracted *Spitzer*/IRAC (CH1 and CH2) postage stamps of MACS1423-z7p64. Black represents positive signal. The source is detected in F125W, F140W and F160W and not detected in any optical bands. The marginal detection in F105W is consistent with a rapid drop in flux around $1.05 \mu\text{m}$, just blue-ward of $\text{Ly}\alpha$. The source is detected in IRAC CH2 but not in CH1. (b) *HST* near-IR false-color image of the galaxy cluster MACS J1423.8+2404 ($z = 0.545$), showing the location of MACS1423-z7p64 (cyan circle) relative to the critical line (white line) and the MOSFIRE slit (yellow rectangle). (c) Close-up of region inside dotted cyan rectangle from (b). The dispersion directions from the two GLASS P.A.s are shown by the red (P.A.= 8°) and white (P.A.= 88°) arrows. (d) Observed broadband flux densities (squares) and 3σ upper limits (downward arrows) from $\sim 0.4 - 5 \mu\text{m}$. Vertical error bars show the 1σ flux density errors and horizontal error bars show the effective width of each filter. We also show the best-fit galaxy spectral energy distributions (SEDs) when redshifts are fixed at the $\text{Ly}\alpha$ redshift $z = 7.640$ (red solid line) and at the hypothetical [O II] redshift $z = 1.818$ (blue dashed line). The flux densities predicted by the best-fit $z = 7.640$ galaxy SED are shown as purple diamonds. The photometric redshift probability density function obtained by allowing the galaxy redshift to vary is shown in the inset in the lower-right corner. The vertical dashed line in the inset marks the $\text{Ly}\alpha$ redshift, $z = 7.640$.

Methods

Imaging Data, Photometry, and Stellar Population Modeling

We use the multi-band *HST* imaging data for MACS J1423.8+2404 from CLASH to constrain the spectral energy distribution (SED) of the galaxy within $\sim 0.4 - 1.7 \mu\text{m}$. CLASH mosaics in $0''.03/\text{pixel}$ are resampled onto a $0''.06/\text{pixel}$ grid before automatic source detection in F160W, and multi-band photometry is performed using SExtractor [24] in dual-image mode. Magnitudes in each *HST* band are measured from the SExtractor ISO magnitude, normalized to the SExtractor AUTO magnitude in F160W. To mitigate contamination from the extended wings of brightest cluster galaxies (BCGs) and intra-cluster light (ICL), we model the BCGs and ICL with smooth light profiles and subtract them from the images following the steps in [25]. Our simulations with artificial sources suggest that for a point source of roughly 25th magnitude, this foreground-subtraction procedure reduces the total flux measurement biases by ~ 0.04 mag in WFC3/IR filters.

Colors between *HST* F160W and *Spitzer*/IRAC $3.6 \mu\text{m}$ and $4.5 \mu\text{m}$ bands are measured from the deep *Spitzer*/IRAC images taken by the *Spitzer* Ultra Faint SURvey Program [26] (SURFSUP). We measure the galaxy’s *Spitzer* flux densities using T-PHOT [27], which employs a template-fitting approach to measure accurate colors between images with different angular resolutions. Empirical *Spitzer*/IRAC point-spread functions (PSFs) are derived from the stacked stellar images within the *Spitzer*/IRAC coverage; these PSFs have full widths at half maximum consistent with those published by the IRAC handbook [26].

From the broadband flux densities measured using the above procedure, we derive constraints on the stellar mass, star formation rate, and dust content of the galaxy by fitting stellar population synthesis model SEDs. We adopt the model SEDs from [28] with the stellar initial mass function from [29] and a constant star formation history. We explored three values of metallicity, $Z = 0.02 Z_{\odot}$, $Z = 0.2 Z_{\odot}$, and $Z = Z_{\odot}$, finding that $Z = 0.02 Z_{\odot}$ produced the best fit to the data. Nebular emission lines and continuum are added to the models based on their Lyman continuum flux as in [30]. We explored two dust attenuation curves, the “SMC” [31] and “Calzetti” [32], finding that the SMC dust attenuation curve provided a better fit to the data. In both models, the stellar and nebular emission are parameterized as in [32] by $E(B - V)_s$ and $E(B - V)_{\text{neb}}$, respectively, related by $E(B - V)_s = 0.44E(B - V)_{\text{neb}}$, and derived from a comparison between Balmer line ratios and the reddening of stellar continua. Larger dust attenuation of the nebular emission relative to the stellar continuum can also be implemented in this way for the SMC dust curve since the SMC and Calzetti dust attenuation curves have very similar shapes at rest-frame optical wavelengths.

The best-fit model SED at the Ly α redshift $z = 7.640$ is shown as the red solid line in Figure 3d, while the bottom-right inset shows the photometric redshift probability distribution when the redshift of the model SED is allowed to vary. We also show the

best-fit model SED at $z = 1.818$ (the hypothetical [O II] redshift) as the blue dashed line, and we find that the $z = 7.640$ solution is strongly favored over the $z = 1.818$ solution.

From the best-fit model SED at $z = 7.640$ and a magnification $\mu = 9.6_{-1.6}^{+1.8}$, we infer the galaxy’s *intrinsic* stellar mass and star formation rate to be $3.0_{-0.8}^{+1.5} \times 10^8 M_{\odot}$ and $13.9_{-3.8}^{+4.2} M_{\odot}/\text{yr}$, respectively, resulting in a sSFR of $46.7_{-17.4}^{+19.0} \text{ Gyr}^{-1}$. Error bars represent 68% confidence intervals that include magnification uncertainty (except for sSFR, which is independent of μ); they are derived from Monte Carlo resampling of the photometry and refitting using the same library of model SEDs [30].

The inferred age of the stellar population is young ($24_{-7}^{+16} \text{ Myr}$), despite a moderate amount of dust extinction at rest-frame 1600 Å ($A_{1600} \approx 1.8 \text{ mag}$ when the SMC curve is used). The combination of very young age and moderate amount of dust extinction has been inferred for other high- z LAEs [11]. Given the inherent degeneracies between age, dust, and metallicity, it is difficult to further constrain these parameters without independent measurements. We experimented with stellar population templates including instantaneous bursts of star formation at various ages (100, 200, 500 and 700 Myr) in combination with the constant star-formation history templates used in our fiducial best-fit SED. The addition of instantaneous burst templates did not result in a better fit to the data than the constant star-formation history templates alone. Therefore, we do not find strong evidence to suggest a hidden, old stellar population for this galaxy.

Gravitational Lens Model of the Galaxy Cluster

The model presented here is a revision of the grid-based lens model of MACS J1423.8+2404 first appearing in [33]. We use the available strong lensing constraints from the previous models as well as improved weak lensing constraints from the *HST* Advanced Camera for Surveys (ACS) F814W filter. Briefly, the lens modeling technique [34, 6] reconstructs the gravitational potential on a non-uniform grid via a χ^2 minimization of strong and weak lensing terms. The method converges much more readily when provided with a reasonable initial model. Our initial model consists of two non-singular isothermal ellipsoids (NIEs) at the locations of the two BCGs and non-singular isothermal spheres (NIS) at the locations of the 10 brightest cluster members within the HST field of view. The velocity dispersions of the two NIEs and NIS cluster members are determined by attempting to broadly reproduce the strong lensing positions. The NIS cluster members are assigned weights based on their F105W magnitudes, whereas the NIE velocity dispersions are chosen individually. We also include in the model a faint ($M_{F105W} = 23.4 \text{ mag}$) galaxy because it is at a small projected separation ($1''.5$) from MACS1423-z7p64. The galaxy likely belongs to the cluster based on its photometric redshift ($z_{\text{phot}} = 0.46 \pm 0.08$). Including this galaxy in the initial model does not significantly affect the fit to the data, but it increases the magnification of MACS1423-z7p64 by $\sim 10\%$. Thus, we include it in the initial model since its effect on MACS1423-z7p64 is significant.

The lens model is constrained by three multiple image systems with spectroscopic

redshifts reported by [35] and one with a photometric redshift identified by [36]. One of the spectroscopic systems is at $z = 1.779$ and the other two are both at $z = 2.84$. The errors on the spectroscopic redshifts were not provided by [35]. The two systems at $z = 2.84$ may be two different knots of the same source, but we include them as two separate systems to increase the number of constraints on the model. We confirm the redshift of the system at $z = 1.779$ with the detection of an emission line at $10370 \pm 50 \text{ \AA}$ in the GLASS spectroscopy of all three images in the system, consistent with [O II] at $z = 1.78 \pm 0.01$. We find no other significant spectral features in the GLASS spectroscopy of these three images or of the other potential images in other systems. The photometric redshift for the final system is $z_{\text{phot}} = 1.97 \pm 0.15$, which we fix to $z = 1.97$ in the model. To generate the weak lensing catalog we use the pipeline described by [37, 38]. The source density of weak lensing galaxies used in the model is $\sim 120 \text{ arcmin}^{-2}$, and the mean ratio of angular diameter distances (β_s) after making a photo- z cut at $z > z_{\text{cluster}} + 0.1$ is $\langle \beta_s \rangle = 0.55 \pm 0.01$ (68% confidence).

The magnification of MACS1423-z7p64 from our model is $9.6_{-2.6}^{+4.3}$ [95% confidence]. Two previous lens models using the same strong lensing constraints are publicly available, which are the Zitrin LTM-Gauss and NFW v2 models [36], and predict the magnification of MACS1423-z7p64 to be $17.2_{-2.5}^{+2.6}$ and $10.6_{-2.0}^{+1.1}$ [95% confidence], respectively. At the 95% confidence level, our model agrees with the NFW v2 model, but disagrees with the LTM-Gauss model. All three models agree that MACS1423-z7p64 is magnified by $\mu \gtrsim 10$. The critical line from our lens model at $z = 7.640$ is shown in Figure 3b. As in our model, MACS1423-z7p64 is outside of the critical line at $z = 7.640$ in the two [36] models, and likely not multiply imaged. However, we search for additional images in the case that MACS1423-z7p64 has a counter-image that is located inside the $z = 7.640$ critical line. No additional images are predicted by any of the models. Throughout this work we adopt the magnification and uncertainties from our model only.

Acknowledgements

AH and this work were supported by NASA Headquarters under the NASA Earth and Space Science Fellowship Program - Grant ASTRO14F-0007. Data presented herein were obtained at the W.M. Keck Observatory, which is operated as a scientific partnership among the California Institute of Technology, the University of California and the National Aeronautics and Space Administration. The Observatory was made possible by the generous financial support of the W.M. Keck Foundation. The authors thank Luca Rizzi and Marc Kassis for help with MOSFIRE observations and data reduction. The authors wish to recognize and acknowledge the very significant cultural role and reverence that the summit of Maunakea has always had within the indigenous Hawaiian community. We are most fortunate to have the opportunity to conduct observations from this mountain. This work is also based on observations made with the NASA/ESA Hubble Space Telescope,

obtained at the Space Telescope Science Institute (STScI), which is operated by the Association of Universities for Research in Astronomy, Inc., under NASA contract NAS5-26555 and NNX08AD79G and ESO-VLT telescopes. Support for GLASS (*HST*-G0-13459) was provided by NASA through a grant from STScI. We are very grateful to the staff of the Space Telescope for their assistance in planning, scheduling and executing the observations, and in setting up the GLASS public release website. Support for this work was also provided by NASA through an award issued by JPL/Caltech and through *HST*-AR-13235, *HST*-GO-13177, *HST*-GO-10200, *HST*-GO-10863, and *HST*-GO-11099 from STScI. Observations were also carried out using the Spitzer Space Telescope, which is operated by the Jet Propulsion Laboratory, California Institute of Technology under a contract with NASA. Support for this work was also provided by NASA through a Spitzer award issued by JPL/Caltech.

Supplementary Information

Reduction and calibration of the Keck/MOSFIRE spectroscopic data

We targeted MACS1423-z7p64 in the Y-band with two distinct multi-object slit-masks, which were created using the MOSFIRE Automatic GUI-based Mask Application (MAGMA). The slit masks used on 27 May, 2015 (PI Bradač; 2.30 hrs) and 19 March 2016 (PI Trenti; 1.85 hrs) had the same position angle, but some of the filler slits differed between the masks. We noticed an astrometric shift of $\sim 0''.1$ between the two mask files created by MAGMA when overlaying them on an *HST* image. This offset is smaller than one MOSFIRE pixel, so we do not expect that it influences our results obtained from stacking the spectra. On 27 May 2015, we employed an ABAB dither pattern with $1''.25$ nod offset, and on 19 March 2016 we employed an ABBA dither pattern also with a $1''.25$ nod offset. The detection of the line in the two independent reductions demonstrates that its origin is not arising from systematic effects associated with dithering. Individual exposures were 180 seconds in duration during both nights, totaling approximately 2.30 hours on 27 May 2015 and 1.85 hours on 19 March 2016. The data from the two nights were reduced using the most updated version of the publicly available MOSFIRE data reduction pipeline (DRP) as of 19 March 2016. The reduction pipeline differences, stacks, and rectifies the nodded images, creating two-dimensional signal and noise spectra for each individual slit. Spectra from individual nights were reduced separately due to varying observing conditions and differences in the positions of the filler slits.

The average seeing was $0''.70$ on 27 May 2015 and $0''.85$ on 19 March 2016 in the J-band. Seeing on 27 May 2015 was calculated solely from the J-band alignment images directly preceding Y-band science observations. The seeing was stable on 27 May 2015 throughout our observations, but less stable on 19 March 2016. A bright star on the 19 March 2016 science mask allowed us to track the seeing in the Y-band during our observations, which we then normalized to the J-band seeing. Because the seeing differed between the two observing nights, we smoothed the 27 May 2015 two-dimensional spectra to match the seeing on 19 March 2016 before combining the spectra. The two individual two-dimensional spectra from the observations on 27 May 2015 and 19 March 2016 were combined by an inverse variance-weighted sum at each pixel. The inverse variance spectra were obtained from the two-dimensional noise spectra produced by the MOSFIRE DRP.

The spectra from 27 May 2015, 19 March 2016, and the inverse variance stack of the two are shown in Supplementary Figure 1. A single emission peak is observed in both the 27 May 2015 spectrum and the 19 March 2016 spectrum. The spatial and spectral location of the peak emission is slightly offset between the two observations despite using the same slit-mask setup. However, the offset is consistent with other emission lines in our slit-mask, once we degrade those emission lines to match the S/N of the Ly α line. The two-dimensional stack shown in the bottom panel of Supplementary Figure 1 differs from

the one shown in Figure 1. Supplementary Figure 1 shows a direct stack, whereas in Figure 1 we show a cross-correlated stack accounting for the observed vertical and horizontal shift. The cross-correlated spectrum is used for the calculation of the line flux and S/N . The observed wavelength of the Ly α line is measured from the stack in Supplementary Figure 1, which does not incorporate any spatial or spectral shifting.

To extract the one-dimensional spectrum from the two-dimensional co-added spectrum, we used an aperture whose size was chosen to enclose $2 \times \text{FWHM}$ of the average seeing during the observations. The one-dimensional spectrum shown in Figure 1 was extracted from the co-added two-dimensional spectrum, so the worse seeing was used to define the aperture size. At each point along the spectral axis, pixels within the spatial aperture were summed with weights determined from a gaussian whose width was also determined by the seeing, producing a one-dimensional spectrum. Flux calibration was done by comparing the one-dimensional extracted spectrum of a standard star we observed to a model spectrum of the same spectral type that was observed on a different night but with comparable atmospheric seeing and transparency. This step takes into account the slit-loss for a point source. Before comparison, we scaled the model spectrum to the apparent magnitude of the observed standard, then correct it for the airmass and galactic extinction of our observations. The ratio of the scaled, corrected model spectrum to the observed telluric spectrum represents the sensitivity function of the telescope.

While the flux calibration corrects for slit-loss from a point-source, we expect that the Ly α emission from MACS1423-z7p64 is more extended [39, 40]. The simplest model for the Ly α spatial distribution is that it traces the rest-frame UV-continuum, sampled by the WFC3/IR filters. From the *HST* F125W, F140W and F160W cutouts in Figure 3a, it is clear that the source is well-resolved. To estimate the flux lost from the slit due to the extended nature of MACS1423-z7p64 (in addition to the point-source term already accounted for), we compare the flux lost from the $0''.7$ MOSFIRE slit for our source versus a point source, both convolved with a Gaussian kernel whose width is determined by the seeing. We model our source with a Sersic profile using GALFIT [41], finding a best-fit Sersic index of ~ 2.7 and effective (half-light) radius of $r_{\text{eff}} \sim 1''$ in F140W, the *HST* filter with the highest S/N. We find a slit-loss correction of 1.6; i.e. we multiply our calibrated flux by this factor to account for the additional flux lost due to the extended nature of the source. This correction has been applied to all MOSFIRE flux and equivalent width values reported in the paper.

Two bright galaxies can be seen near the top of the slit in Figure 3c. Their traces contaminate both spectra at approximately the same vertical position as the top negative residual from the emission line. We subtracted these traces and their negative residuals by calculating the average pixel value in each row of the reduced two-dimensional spectrum from each night separately. The spectra shown in the top two panels of Supplementary Figure 1 are post-subtraction. The co-added spectrum shown in the bottom panel of Supplementary Figure 1 was obtained from the trace-subtracted individual spectra.

In principle, the continuum from this galaxy could be detected by binning over a

sufficiently large bandpass. We note that the negative signals of the aforementioned contaminating galaxies are larger than the continuum predicted from the measured F125W HST flux, which is red-ward of Ly α without containing any flux from the Ly α line itself. We nonetheless checked for continuum from MACS1423-z7p64 by comparing the means of the one-dimensional spectrum red-ward and blue-ward of the Ly α emission before subtraction of the contamination. When computing the means, we used approximately the same size bandpass red-ward and blue-ward of Ly α ($\sim 550\text{\AA}$). Before computing the means we clip off $\sim 10\%$ from both ends of the distributions to reject sky line contamination. We do not measure a statistically larger mean red-ward than blue-ward of Ly α , which is evidence that we are not detecting the continuum from MACS1423-z7p64. This is not surprising given the level of the contamination compared to the expected continuum signal.

The S/N of the emission line was determined from the one-dimensional spectrum shown in Figure 1. S is the flux of the line and N is the RMS noise summed in quadrature over the same bandpass used to determine the flux, which is $10501 - 10510\text{\AA}$. The line flux is $0.41 \pm 0.06 \times 10^{-17} \text{ erg/s/cm}^2$, resulting in a $S/N = 6.7$ detection. The bandpass is limited on the red side due to the sky line as shown in Figure 1. The sky line renders an asymmetry test unreliable and also potentially reduces the line flux we are able to measure. The Ly α detection is not sensitive to the pixel contributing a significant amount of flux just blueward of the sky line in Figure 1; the S/N is 6.0 if this pixel is not included in the bandpass. The emission line at 10504\AA is the only $S/N > 5$ feature within the $\pm 50\text{\AA}$ window from GLASS that appears in both the 27 May 2015 and 19 Mar 2016 spectra.

Description of the GLASS data

GLASS is an *HST* large program that targeted 10 massive galaxy clusters during Cycle 21 [3, 4]. Data were taken with the WFC3 G102 and G141 grisms in the cluster cores and the ACS G800L grism in parallel fields. Because we focus on the cluster core in this work, we only use the data from the WFC3 grisms. 14 orbits were allocated for each cluster, distributed to achieve uniform sensitivity over the range in wavelengths $0.8 - 1.7\mu m$. Each cluster was observed at two position angles (P.A.s) approximately 90 degrees apart to aid in contamination subtraction. The two GLASS P.A.s for MACS J1423.8+2404 (P.A.= 8° and P.A.= 88°) are shown in Figure 3c.

The spectral extraction for MACS1423-z7p64 we performed is similar to that described by [1], but with two important differences that resulted in a slight enhancement in the S/N of the Ly α emission line ($S/N = 2.4$ in this work versus $S/N = 2.1$ from [1]). First, we used an updated reduction of the GLASS data. This is based on a more reliable detection and flux scaling of contaminating sources affecting the flux levels and noise properties of the contamination-subtracted spectra from which the line flux is estimated. Second, we force-extracted the spectrum at the exact coordinates of the source, and in doing so assumed a circular aperture for contamination modeling. In [1], we extracted the spectra using SExtractor-defined segmentation maps of the nearest matches to the coordinates of

the object.

The G102 and G141 spectra at both P.A.s are shown in Figure 2. Ly α is detected marginally at $S/N = 2.4$ in the P.A. = 88° G102 spectrum at $10500 \pm 50 \text{ \AA}$, implying a redshift of $z = 7.64 \pm 0.04$, in agreement with the redshift measured with Keck/MOSFIRE. The inferred Ly α equivalent width from GLASS is $W_{\text{Ly}\alpha} = 27 \pm 11 \text{ \AA}$. Because the continuum was not detected in the spectrum, the continuum flux density used for the equivalent width measurement was estimated from the broadband *HST* flux in the F125W band. This band was chosen because it samples the rest-frame UV continuum near the Ly α wavelength without containing any contribution from the Ly α emission or the Ly α break.

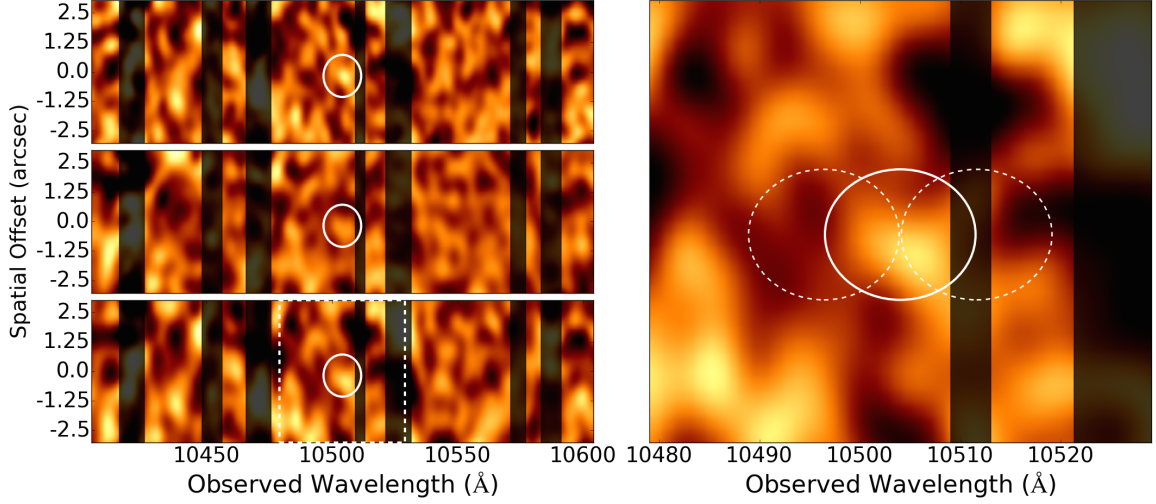
The G141 spectral coverage allows us to search for additional emission lines at $z = 7.640 \pm 0.001$, such as C IV $\lambda\lambda 1548, 1551$ and C III] $\lambda\lambda 1907, 1909$, both of which would be blended in the GLASS spectroscopy. No significant spectral features were recovered from this search. The 3σ limits on the fluxes and equivalent widths for C IV and C III] are shown in Table 1. The continuum flux densities used to determine the equivalent widths were estimated in a similar manner to the Ly α equivalent width measurement described above, but instead the F160W and F140W filter fluxes were used for C IV and C III], respectively.

Nominally, the Ly α flux derived from the grism is a factor of ~ 3 larger than the Keck/MOSFIRE flux. However, the grism-derived flux we report in Table 1 was obtained using an aperture designed to optimize the signal to noise ratio (S/N) of the line, whereas the aperture of the MOSFIRE observations is fixed by the size of the slit, $0''.7$. Once the apertures are matched, the fluxes from the grism and MOSFIRE agree within the uncertainties. Higher levels of contamination are the most likely cause for the non-detection of Ly α in P.A. = 8° of the grism.

Alternative interpretations of the emission line

We find that the most likely interpretation of the emission line is Ly α at $z = 7.640$. However, we explore the next most likely scenario in which the line is [O II] $\lambda\lambda 3726, 3729$ at $z = 1.818$. The strong break observed in the photometry at $\sim 1.05 \mu m$ rules out emission lines other than Ly α and [O II] since it is either the Lyman or Balmer break. The resolution of MOSFIRE is sufficient to resolve the [O II] doublet at $z = 1.818$. Supplementary Figure 1 shows the expected locations of the 3726 \AA and 3729 \AA lines in the [O II] doublet if the emission line observed at $\sim 10504 \text{ \AA}$ was the 3729 \AA line or the 3726 \AA line, respectively. If the line at $\sim 10504 \text{ \AA}$ was the 3729 \AA line, then the bluer 3726 \AA line would have been observed since it falls in a region free of strong sky emission lines. The typical $3729 \text{ \AA} / 3726 \text{ \AA}$ intensity ratio for star-forming galaxies is 1.5/1, so the 3726 \AA line would have been detected in this case. If the line at $\sim 10504 \text{ \AA}$ was the 3726 \AA line, then the redder 3729 \AA line would have fallen on a sky line and would therefore have been undetectable.

The strongest evidence against the line being [O II] comes from the grism observations. The GLASS grism spectra cover the [O III] pair in the case where the emission line at $\sim 10504 \text{ \AA}$ is [O II]. However, the [O III] pair is not detected in either P.A. (Figure 2),



Supplementary Figure 1: Two-dimensional signal spectra from the (**Top left**) 2.30 hr 27 May 2015 observation, (**Middle left**) 1.85 hr 19 March 2016 observation and (**Bottom left**) direct inverse-variance stack of the two spectra. The emission line, which we are confident is the Ly α line, is circled in white in all panels. (**Right**) Zoomed in region on the emission line from the stacked spectrum shown in the bottom left panel. Again, the emission line at 10504Å is circled in white. The dotted circle to the left (right) of the emission line shows the expected location of the 3726Å (3729Å) line in the [O II] $\lambda\lambda$ 3726, 3279Å doublet if the observed emission line was instead the 3729Å (3726Å) line at $z = 1.818$. The observed emission line at 10504Å cannot be the 3729Å line because we would have detected the bluer 3726Å line in that case. In the case that the observed emission line at 10504Å was the 3726Å line, the sky line would have obscured the 3729Å line. The grism spectra provide strong evidence against the [O II] interpretation of the line, however. The spectra in all panels have been smoothed to the average seeing of each observation using a circular Gaussian kernel.

resulting in a 2σ upper limit of $f_{[\text{O III}]} / f_{[\text{O II}]} < 0.65$ in P.A.=88°. At $z = 1.818$, the galaxy would have an intrinsic stellar mass of $\sim 1 \times 10^9 M_{\odot}$, which would imply $f_{[\text{O III}]} / f_{[\text{O II}]} \geq 1.5$ [23], inconsistent with our observations. Furthermore, the SED fitting strongly prefers the $z = 7.640$ solution ($\chi^2_{\nu} = 0.9$) over the $z = 1.818$ solution ($\chi^2_{\nu} = 3.4$). In summary, we are confident that the line at $\sim 10504\text{Å}$ is not [O II] and therefore must be Ly α .

References

- [1] Schmidt, K. B. *et al.* The Grism Lens-Amplified Survey from Space (GLASS). III. A Census of Ly α Emission at $z \gtrsim 7$ from HST Spectroscopy. *Astrophys. J.* **818**, 38 (2016). 1511.04205.

- [2] Postman, M. *et al.* The Cluster Lensing and Supernova Survey with Hubble: An Overview. *Astrophys. J Suppl. Ser.* **199**, 25 (2012). 1106.3328.
- [3] Schmidt, K. B. *et al.* Through the Looking GLASS: HST Spectroscopy of Faint Galaxies Lensed by the Frontier Fields Cluster MACSJ0717.5+3745. *Astrophys. J.* **782**, L36 (2014). 1401.0532.
- [4] Treu, T. *et al.* The Grism Lens-Amplified Survey from Space (GLASS). I. Survey Overview and First Data Release. *Astrophys. J.* **812**, 114 (2015). 1509.00475.
- [5] McLean, I. S. *et al.* MOSFIRE, the multi-object spectrometer for infra-red exploration at the Keck Observatory. In *Ground-based and Airborne Instrumentation for Astronomy IV*, vol. 8446 of *Proc. SPIE*, 84460J (2012).
- [6] Bradač, M. *et al.* Focusing Cosmic Telescopes: Exploring Redshift $z \sim 5$ -6 Galaxies with the Bullet Cluster 1E0657 - 56. *Astrophys. J.* **706**, 1201–1212 (2009). 0910.2708.
- [7] Bouwens, R. J. *et al.* UV Luminosity Functions at Redshifts $z \sim 4$ to $z \sim 10$: 10,000 Galaxies from HST Legacy Fields. *Astrophys. J.* **803**, 34 (2015). 1403.4295.
- [8] Schenker, M. A. *et al.* Keck Spectroscopy of Faint $3 < z < 8$ Lyman Break Galaxies: Evidence for a Declining Fraction of Emission Line Sources in the Redshift Range $6 < z < 8$. *Astrophys. J.* **744**, 179 (2012). 1107.1261.
- [9] Treu, T., Schmidt, K. B., Trenti, M., Bradley, L. D. & Stiavelli, M. The Changing Ly α Optical Depth in the Range $6 < z < 9$ from the MOSFIRE Spectroscopy of Y-dropouts. *Astrophys. J.* **775**, L29 (2013). 1308.5985.
- [10] Pentericci, L. *et al.* New Observations of $z \sim 7$ Galaxies: Evidence for a Patchy Reionization. *Astrophys. J.* **793**, 113 (2014). 1403.5466.
- [11] Finkelstein, S. L. *et al.* A galaxy rapidly forming stars 700 million years after the Big Bang at redshift 7.51. *Nature* **502**, 524–527 (2013). 1310.6031.
- [12] Oesch, P. A. *et al.* A Spectroscopic Redshift Measurement for a Luminous Lyman Break Galaxy at $z = 7.730$ Using Keck/MOSFIRE. *Astrophys. J.* **804**, L30 (2015). 1502.05399.
- [13] Zitrin, A. *et al.* Lyman α Emission from a Luminous $z = 8.68$ Galaxy: Implications for Galaxies as Tracers of Cosmic Reionization. *Astrophys. J.* **810**, L12 (2015). 1507.02679.
- [14] Song, M. *et al.* Keck/MOSFIRE Spectroscopy of $z=7$ -8 Galaxies: Ly α Emission from a Galaxy at $z=7.66$. *ArXiv e-prints* (2016). 1602.02160.

- [15] Castellano, M. *et al.* First Observational Support for Overlapping Reionized Bubbles Generated by a Galaxy Overdensity. *Astrophys. J.* **818**, L3 (2016). 1601.03442.
- [16] Bauer, A. *et al.* Hydrogen reionization in the Illustris universe. *Mon. Not. R. Astron. Soc.* **453**, 3593–3610 (2015). 1503.00734.
- [17] Hutter, A., Dayal, P., Müller, V. & Trott, C. Exploiting 21cm - Ly α emitter synergies: constraints on reionization. *ArXiv e-prints* (2016). 1605.01734.
- [18] Wyithe, J. S. B. & Loeb, A. A characteristic size of ~ 10 Mpc for the ionized bubbles at the end of cosmic reionization. *Nature* **432**, 194–196 (2004). astro-ph/0409412.
- [19] Labbé, I. *et al.* The Spectral Energy Distributions of $z \sim 8$ Galaxies from the IRAC Ultra Deep Fields: Emission Lines, Stellar Masses, and Specific Star Formation Rates at 650 Myr. *Astrophys. J.* **777**, L19 (2013). 1209.3037.
- [20] Roberts-Borsani, G. W. *et al.* $z \gtrsim 7$ Galaxies with Red Spitzer/IRAC [3.6]-[4.5] Colors in the Full CANDELS Data Set: The Brightest-Known Galaxies at $z \sim 7 - 9$ and a Probable Spectroscopic Confirmation at $z = 7.48$. *Astrophys. J.* **823**, 143 (2016). 1506.00854.
- [21] Nakajima, K. *et al.* A Hard Ionizing Spectrum in $z=3-4$ Ly-alpha Emitters with Intense [OIII] Emission: Analogs of Galaxies in the Reionization Era? *ArXiv e-prints* (2016). 1608.08222.
- [22] Stark, D. P. *et al.* Lyman-alpha and CIII] Emission in $z=7-9$ Galaxies: Accelerated Reionization Around Luminous Star Forming Systems? *ArXiv e-prints* (2016). 1606.01304.
- [23] Henry, A. *et al.* Low Masses and High Redshifts: The Evolution of the Mass-Metallicity Relation. *Astrophys. J.* **776**, L27 (2013). 1309.4458.
- [24] Bertin, E. & Arnouts, S. SExtractor: Software for source extraction. *Astron. Astrophys. Suppl. Ser.* **117**, 393–404 (1996).
- [25] Merlin, E. *et al.* The ASTRODEEP Frontier Fields catalogues. I. Multiwavelength photometry of Abell-2744 and MACS-J0416. *Astron. Astrophys.* **590**, A30 (2016). 1603.02460.
- [26] Bradač, M. *et al.* Spitzer Ultra Faint SURvey Program (SURFS UP). I. An Overview. *Astrophys. J.* **785**, 108 (2014). 1402.2352.
- [27] Merlin, E. *et al.* T-PHOT: A new code for PSF-matched, prior-based, multiwavelength extragalactic deconfusion photometry. *Astron. Astrophys.* **582**, A15 (2015). 1505.02516.

- [28] Bruzual, G. & Charlot, S. Stellar population synthesis at the resolution of 2003. *Mon. Not. R. Astron. Soc.* **344**, 1000–1028 (2003). [astro-ph/0309134](#).
- [29] Chabrier, G. Galactic Stellar and Substellar Initial Mass Function. *Publ. Astron. Soc. Pacific* **115**, 763–795 (2003). [astro-ph/0304382](#).
- [30] Huang, K.-H. *et al.* Spitzer Ultra Faint SURvey Program (SURFS UP). II. IRAC-detected Lyman-Break Galaxies at $6 \lesssim z \lesssim 10$ behind Strong-lensing Clusters. *Astrophys. J.* **817**, 11 (2016). [1504.02099](#).
- [31] Pei, Y. C. Interstellar dust from the Milky Way to the Magellanic Clouds. *Astrophys. J.* **395**, 130–139 (1992).
- [32] Calzetti, D. *et al.* The Dust Content and Opacity of Actively Star-forming Galaxies. *Astrophys. J.* **533**, 682–695 (2000). [astro-ph/9911459](#).
- [33] Vulcani, B. *et al.* The Grism Lens-Amplified Survey from Space (Glass). V. Extent and Spatial Distribution of Star Formation in $Z \sim 0.5$ Cluster Galaxies. *Astrophys. J.* **814**, 161 (2015). [1511.00686](#).
- [34] Bradač, M., Schneider, P., Lombardi, M. & Erben, T. Strong and weak lensing united. I. The combined strong and weak lensing cluster mass reconstruction method. *Astron. Astrophys.* **437**, 39–48 (2005).
- [35] Limousin, M. *et al.* MACS J1423.8+2404: gravitational lensing by a massive, relaxed cluster of galaxies at $z = 0.54$. *Mon. Not. R. Astron. Soc.* **405**, 777–782 (2010). [0911.4125](#).
- [36] Zitrin, A. *et al.* Hubble Space Telescope Combined Strong and Weak Lensing Analysis of the CLASH Sample: Mass and Magnification Models and Systematic Uncertainties. *Astrophys. J.* **801**, 44 (2015). [1411.1414](#).
- [37] Schrabback, T. *et al.* Evidence of the accelerated expansion of the Universe from weak lensing tomography with COSMOS. *Astron. Astrophys.* **516**, A63 (2010). [0911.0053](#).
- [38] Schrabback, T. *et al.* Cluster Mass Calibration at High Redshift: HST Weak Lensing Analysis of 13 Distant Galaxy Clusters from the South Pole Telescope Sunyaev-Zel'dovich Survey. *ArXiv e-prints* (2016). [1611.03866](#).
- [39] Steidel, C. C. *et al.* Diffuse Ly α Emitting Halos: A Generic Property of High-redshift Star-forming Galaxies. *Astrophys. J.* **736**, 160 (2011). [1101.2204](#).
- [40] Wisotzki, L. *et al.* Extended Lyman α haloes around individual high-redshift galaxies revealed by MUSE. *Astron. Astrophys.* **587**, A98 (2016). [1509.05143](#).

- [41] Peng, C. Y., Ho, L. C., Impey, C. D. & Rix, H.-W. Detailed Decomposition of Galaxy Images. II. Beyond Axisymmetric Models. *Astron. J.* **139**, 2097–2129 (2010). 0912.0731.